Chapter 6
Modeling of Hydrogen Diffusion in Slow Strain Rate (SSR) Testing of Notched Samples

Andreas Drexler, Josef Domitner, and Christof Sommitsch

Abstract Macroscopic testing of the hydrogen embrittlement (HE) resistivity of ultra and advanced high-strength steels is still a difficult task. Different testing procedures are recommended in literature, such as the slow strain rate (SSR) test, the constant load (CL) test, or the incremental step load (ISL) test. Nevertheless, a direct comparison of the results of the different testing procedures is challenging and the influence of the microstructure is not well understood. Therefore, the present work contributes to a deeper understanding of the role of internal hydrogen diffusion and trapping at microstructural defects during SSR testing of notched samples using physical reasonable diffusion-mechanical finite element (FE) simulations. The modeling approach allows a detailed study of the role of macroscopic strength and multiple trapping sites on the local hydrogen accumulation at the notch.

Keywords Hydrogen diffusion · Beneficial trapping · Hydrogen embrittlement · Slow strain rate testing · Notch effect

6.1 List of Symbols

A	mm^2	Sample surface area
c	wppm	Total hydrogen concentration
c_{im}	wppm	Immobile hydrogen concentration
c_L	wppm	Lattice hydrogen concentration
$c_{L,0}$	wppm	Lattice hydrogen concentration under zero hydrostatic stress
$c_{T,i}$	wppm	Trapped hydrogen concentration
D_{chem}	mm^2/s	Chemical diffusion coefficient
D_L	mm^2/s	Tracer diffusion coefficient

A. Drexler (✉) · J. Domitner · C. Sommitsch
Institute of Materials Science, Joining and Forming (IMAT), Graz University of Technology (TU Graz), Inffeldgasse 11/I, 8010 Graz, Austria
e-mail: andreas.drexler@tugraz.at

V. A. Polyanskiy and A. K. Belyaev (eds.), *Advances in Hydrogen Embrittlement Study*, Advanced Structured Materials 143, https://doi.org/10.1007/978-3-030-66948-5_6

E	GPa	Young's modulus
$E_{\mathrm{B,i}}$	kJ/mol	Binding energy of traps
$E_{\mathrm{B,deep}}$	kJ/mol	Binding energy of deep trapping sites of 60 kJ/mol
$E_{\mathrm{B,shallow}}$	kJ/mol	Binding energy of shallow trapping sites of 30 kJ/mol
E_{S}	kJ/mol	Solution enthalpy
$\varepsilon_{\mathrm{eng}}$	−	Engineering strain
$\varepsilon_{\mathrm{pl}}$	−	Equivalent plastic strain
$\varepsilon_{\mathrm{eqv}}$	−	Equivalent strain
γ	mm^{-2}	Correlation factor between dislocation density and equivalent plastic strain
J	$\mathrm{mol/mm^2 s}$	Total hydrogen flux
$J_{\nabla \mathrm{c}}$	$\mathrm{mol/mm^2 s}$	Chemical hydrogen flux
$J_{\nabla \sigma}$	$\mathrm{mol/mm^2 s}$	Stress-driven hydrogen flux
K	MPa	Strength coefficient
K_{i}	−	Equilibrium constant of trapping sites i
$K_{\nabla \sigma}$	−	Equilibrium constant for volumetric strained interstitial lattice sites
k	mol/mm	Number of shallow trap sites per unit dislocation length
L_0	mm	Length of the unstrained gauge section of a sample
L	mm	Length of the strained gauge section of a sample
l	mm	Size of the plastic zone
m	$\mathrm{wppm/MPa^{1/2}}$	Constant factor of Sievert's law
M_{H}	g/mol	Molar mass of hydrogen
μ_{L}	kJ/mol	Chemical potential of the lattice hydrogen in bulk
$\mu_{\mathrm{P_{H_2}}}$	kJ/mol	Chemical potential of the gaseous hydrogen molecules
N	−	Total number of trapping sites
N_{L}	$\mathrm{mol/mm^3}$	Density of interstitial lattice sites
$N_{\mathrm{T,0}}$	$\mathrm{mol/mm^3}$	Initial trap density
$N_{\mathrm{T,i}}$	$\mathrm{mol/mm^3}$	Trap density of trapping sites *i*
n	−	Strain hardening exponent
ν	−	Poisson constant
$p_{\mathrm{H_2}}$	MPa	Hydrogen partial pressure
R_{g}	J/molK	Universal gas constant
ρ	$\mathrm{g/mm^3}$	Density
σ_{H}	MPa	Hydrostatic stress
σ_{Mises}	MPa	Von Mises stress
σ_{y}	MPa	Yield stress
$\sigma_{\mathrm{y,0}}$	MPa	Initial yield stress
T	K	Temperature
t	s	Hydrogen charging time
V	$\mathrm{mm^3}$	Sample volume
V_{H}	$\mathrm{mm^3/mol}$	Partial molar volume of hydrogen
$y_{\mathrm{T,i}}$	−	Site fraction of trapping sites *i*
y_{L}	−	Lattice site fraction

6.2 Introduction

Hydrogen in metals, especially in advanced high-strength steels, can cause premature macroscopic brittle failure [1]. Different test procedures for dog bone-shaped samples are available to investigate the susceptibility of the microstructure to hydrogen embrittlement ranging from constant load (CL) tests to slow strain rate (SSR) tests. The incremental step load (ISL) tests combine aspects of both SSR and CL tests. Comparing the susceptibility of different materials to hydrogen embrittlement (HE) or testing under real hydrogen donating conditions coined the terms "internal" hydrogen embrittlement (IHE), hydrogen "environmental" embrittlement (HEE), and hydrogen-induced stress corrosion cracking (SCC). Lynch [2] has already stated that the hydrogen source can trigger different embrittlement sites within the microstructure. It may change the rate-controlled process from hydrogen diffusion to hydrogen adsorption by controlling the kinetics of IHE and HEE. The distinction between IHE, HEE, or SCC makes sense from an experimental macroscopic point of view, however, the microscopic HE mechanisms [3, 5–7] do not distinguish different hydrogen sources. Evaluation of the material susceptibility to hydrogen embrittlement is often done by comparing time to failure and threshold stresses, which are measured with CL or SSR tests. However, both quantities are also influenced by other factors than microstructure, like

1. hydrogen charging procedure,
2. sample geometry,
3. strain rate, and
4. applied mechanical load.

This indicates a strong dependency of the time to failure and threshold stress on hydrogen absorption, diffusion, and hydrogen accumulation in critical zones [8]. Therefore, the roles of internal hydrogen diffusion and trapping in SSR testing of hydrogen pre-charged and notched samples must be investigated. For that purpose, a physically reasonable, fully coupled diffusion-mechanical finite element (FE) model [9] was developed and parametrized. Using this FE model, the roles of

1. competitive mechanisms of stress-driven hydrogen diffusion and shallow hydrogen trapping by means of local plastic deformation,
2. "beneficial" deep trapping sites,
3. strain rate dependency,
4. mechanical strength, and
5. strain hardening

on the local hydrogen accumulation at the notch are studied in detail.

6.3 Multiphysical Modeling of Slow Strain Rate (SSR) Tests

It is well known that hydrostatic stresses and plastic strain have a crucial effect on the macroscopic hydrogen accumulation at the notch [10]. For that purpose, the fully coupled diffusion-mechanical model of Barrera et al. [9] was implemented in the FE software package Abaqus [11] using the UMATHT subroutine. Barrera has shown how to compute directly the gradient of hydrostatic stress field inside the UMATHT using common block variables with USDFLD and GETVRM subroutines and how to consider hydrogen trapping on the overall chemical diffusion [10, 12].

6.3.1 Sample Geometry and Finite Element Meshing

A notched 1-mm thick sample was studied with a notch radius of 0.1 mm and a notch angle of 60°, as shown in Fig. 6.1a. The initial length of the gauge section was 60 mm. Due to symmetry conditions, only a quarter of the sample was meshed with 8-node plane stress diffusionally coupled quadrilateral elements (CPS8T). The minimum mesh size was 1 μm directly at the notch root, while the maximum mesh size was 0.5 mm at the top side of the sample, as shown in Fig. 6.1b.

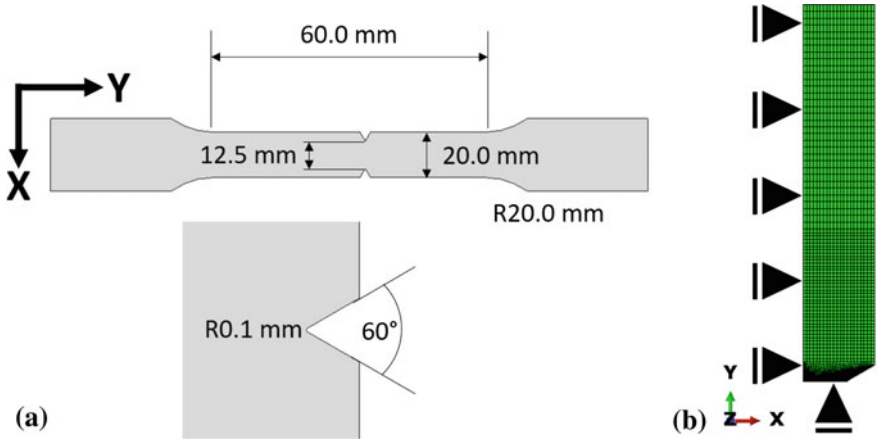

Fig. 6.1 **a** Sketch of the notched sample considered in the multiphysical FE model. **b** Due to symmetry conditions, only a quarter of the sample was modeled

6.3.2 Mechanical Material Modeling

Linear elastic-plastic material behavior with isotropic material hardening was considered. The yield condition was expressed as

$$\sigma_{\text{Mises}} = \sigma_y, \tag{6.1}$$

where σ_{Mises} is the von Mises stress and σ_{y} is the yield stress. The evolution of the yield stress with plastic deformation is defined as the sum of the initial yield stress $\sigma_{\text{y,0}}$ and the hardening function, according to Hollomon and Ludwik,

$$\sigma_{\text{y}} = \sigma_{\text{y,0}} + K\varepsilon_{\text{pl}}^{n}\,, \tag{6.2}$$

where K is the strength coefficient and n is the strain hardening exponent. ε_{pl} is the equivalent plastic strain. Neither a strain rate dependency of the material hardening, as observed in advanced high-strength steels at low temperatures [13], nor softening [9] with increasing hydrogen concentration was considered in the present study. Furthermore, the presented model does not consider the influence of damage by means of micropores or microcracks on the hydrogen accumulation during SSR testing [8, 14].

6.3.3 Diffusional Modeling of Lattice Hydrogen

The total hydrogen flux J is the sum of the chemical hydrogen flux $J_{\nabla c}$ driven by the hydrogen concentration gradient according to Fick's first law and the stress-driven hydrogen flux $J_{\nabla\sigma}$ [15]:

$$J = J_{\nabla \text{c}} + J_{\nabla\sigma} = -D_{\text{L}}\nabla c_{\text{L}} + \frac{D_{\text{L}}c_{\text{L}}V_{\text{H}}}{R_{\text{g}}T}\nabla\sigma_{\text{H}}. \tag{6.3}$$

In Eq. (6.3), D_{L} is the tracer diffusion coefficient of the interstitial lattice sites, c_{L} is the lattice hydrogen concentration, V_{H} is the partial molar volume of hydrogen, R_{g} is the universal gas constant, and T is the temperature. The hydrostatic stress is defined as $\sigma_{\text{H}} = \frac{1}{3}(\sigma_{11} + \sigma_{22} + \sigma_{33})$. Pipe diffusion [16] of hydrogen, e.g., along dislocation networks, or grain boundary diffusion was not considered in the diffusion model, because of its negligible influence in bcc iron [17]. This assumption was also confirmed by Siegl et al. [18] studying the influence of the grain size and plastic deformation on the chemical hydrogen diffusion in bcc iron for industrial relevant grain sizes of (10 µm and larger).

6.3.4 Hydrogen Micro-segregation Modeling

Mass conservation requires that the total hydrogen flux through the surfaces of an element is equal to the change of total hydrogen concentration within this element. The total hydrogen concentration c is the sum of the interstitial lattice hydrogen concentration c_L, the reversible trapped hydrogen concentration $c_{T,i}$ at microstructural defects i and the immobile hydrogen concentration c_{im}:

$$c = c_L + \sum_{i=1,N} c_{T,i} + c_{im}. \tag{6.4}$$

N is the total number of reversible trapping sites within the microstructure. Figure 6.2 illustrates the hydrogen energy states of the microstructure with respect to the concentrations of lattice hydrogen, reversible trapped hydrogen, and immobile hydrogen.

Lattice hydrogen occupies interstitial lattice positions, such as tetragonal sites in bcc iron [19, 20], which provides fast diffusion paths between neighboring reversible trapping sites. In ferrite activation energies of lattice hydrogen diffusion from 5 kJ/mol to 10 kJ/mol [21–24] are reported, which enable hydrogen exchange between neighboring reversible trapping sites (mean free distance of approximately 1 nm) within nanoseconds or less. The direct exchange between lattice hydrogen and reversible trapped hydrogen can be expressed in the following reaction equation as

$$H_L + V_T \leftrightharpoons V_L + H_T. \tag{6.5}$$

H_L are interstitial lattice hydrogen atoms, V_T are vacant reversible trapping sites, V_L are vacant interstitial lattice sites, and H_T are reversibly trapped hydrogen atoms. Hydrogen trapping at microstructural defects does not alter the microstructure and can be regarded as a reversible reaction. According to Toribio and Kharin [25]

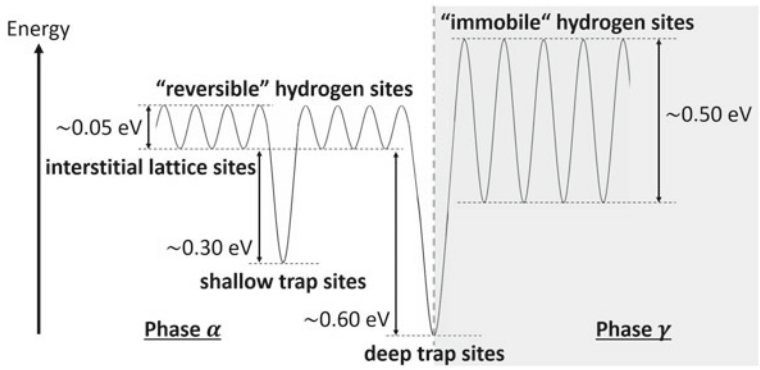

Fig. 6.2 Schematic illustration of the hydrogen energy states of the microstructure considered in this work

equilibrium between lattice hydrogen and trapped hydrogen is locally reached, if the time for long-range hydrogen diffusion is much larger than the characteristic time for local relaxation between interstitial lattice hydrogen and trapped hydrogen. Applying the generalized Oriani's [26] equation relates the site fraction of reversible trapped hydrogen $y_{\mathrm{T,i}} = c_{\mathrm{T,i}}/N_{\mathrm{T,i}}$ to the site fraction of lattice hydrogen $y_{\mathrm{L}} = c_{\mathrm{L}}/N_{\mathrm{L}}$:

$$\frac{y_{\mathrm{L}}(1 - y_{\mathrm{T,i}})}{y_{\mathrm{T,i}}(1 - y_{\mathrm{L}})} = \exp\left(-\frac{E_{\mathrm{B,i}}}{R_{\mathrm{g}}T}\right) = K_{\mathrm{i}}. \tag{6.6}$$

N_{L} is the density of interstitial lattice sites and $N_{\mathrm{T,i}}$ is the trap density. K_{i} is the equilibrium constant and $E_{\mathrm{B,i}}$ is the binding energy of the reversible trapping sites i. Reversible trapping sites provide a variety of binding energies ranging up to approximately 100 kJ/mol. Immobile hydrogen differs from reversible trapped hydrogen according to its expansion in the microstructure and to its activation energy for local hydrogen diffusion. The concept is new to the authors' knowledge and differs from the often cited theory of "quasi-irreversible" trapped hydrogen [27]. Immobile hydrogen occupies interstitial lattice sites in secondary phases with very low diffusion rates at room temperature, e.g., retained austenite or titanium carbides [28, 29]. The activation energy for local hydrogen diffusion in retained austenite or in carbides is reported as 50 kJ/mol or higher [29, 30]. Phase transformation or thermal activation at elevated temperatures release the immobile hydrogen to the matrix.

6.3.5 Constitutive Modeling of Trap Density Evolution

Microstructural defect densities and the density of reversible hydrogen trapping sites $N_{\mathrm{T,i}}$ evolve during industrial thermomechanical processing of a material:

1. Heat treatments at elevated temperatures [31–34] cause growth and coarsening of carbides, which change the number of available trapping sites at the interfaces between carbides and matrix [28, 35].
2. Cold forming is the main factor at room temperature changing the reversible trap densities in the material by increasing vacancy and dislocation densities [17, 36].

A further constitutive equation for the evolution of the trap density N_{T} with equivalent plastic deformation is [17]

$$N_{\mathrm{T}} = N_{\mathrm{T,0}} + k\gamma\varepsilon_{\mathrm{pl}}, \tag{6.7}$$

with $N_{\mathrm{T,0}}$ being the initial trap density and k and γ being semi-empirical material constants. Figure 6.3 compares Eq. (6.7) with respect to other evolution equations suggested in literature [10, 17, 37–39]. The trap densities introduced by plastic deformation cover a range of 10^{-13}–10^{-5} mol/mm^3. The evolution equations and material constants derived by Song et al. [37] and Drexler et al. [17] agree very well.

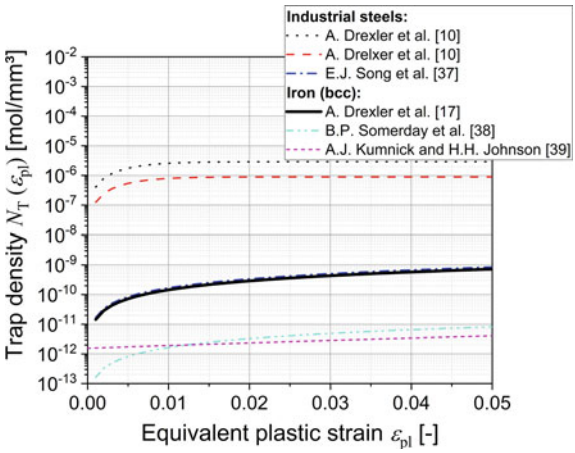

Fig. 6.3 The hydrogen trap density increases with increasing equivalent plastic strain

6.4 Model Parametrization

To apply the diffusion-mechanical FE model for SSR testing, mechanical and diffusional model parameters have to be defined. The identification of mechanical model parameters is well established in literature and can be based on classical tensile tests. The parametrization of Eq. (6.2) allows to extrapolate the stress–strain behavior also to larger equivalent plastic strain. In this study, all simulation results are referenced to the yield curve with $\sigma_{y,0} = 1000$ MPa, $K = 1200$ MPa and $n = 0.5$. This "reference" yield curve is indicated by a bold black line in Fig. 6.4a, b. To study the influence of the initial yield stress on the SSR tests, $\sigma_{y,0}$ was increased from 600 MPa to 1400 MPa with $K = 1200$ MPa and $n = 0.5$, as shown in Fig. 6.4a. To study the effect of strain hardening on the local hydrogen accumulation at the notch, K was increased from 0 MPa (ideal plastic deformation) to 1900 MPa, as shown in Fig. 6.4b, while $\sigma_{y,0} = 1000$ MPa and $n = 0.5$.

The identification of the diffusional model parameters is a difficult task, especially for a broad application range. The diffusional material parameters of the lattice hydrogen (D_L, N_L) were measured by electrochemical permeation on well-annealed bcc iron samples. Appropriate permeation samples need a minimum thickness of 1–2 mm and palladium coatings, especially on the oxidation sides [18, 21] to reduce the influence of surface reactions and hydrogen recombination. Assuming that the samples were nearly trap-free allows to determine the tracer hydrogen diffusion coefficient D_L and the density of the interstitial lattice sites N_L. A previous literature survey revealed $D_L = 9 \cdot 10^{-3}$ mm^2/s for well-annealed iron at room temperature [40]. This value was confirmed by Siegl et al. [18]. The results from electrochemical permeation measurements, especially the activation energy of lattice hydrogen diffusion, are in good agreement with DFT calculations [41] representing ideal defect-free iron crystals. The trapping parameters, as the total number of trapping sites N, and the corresponding binding energies $E_{B,i}$ and trap densities $N_{T,i}$, can be identi-

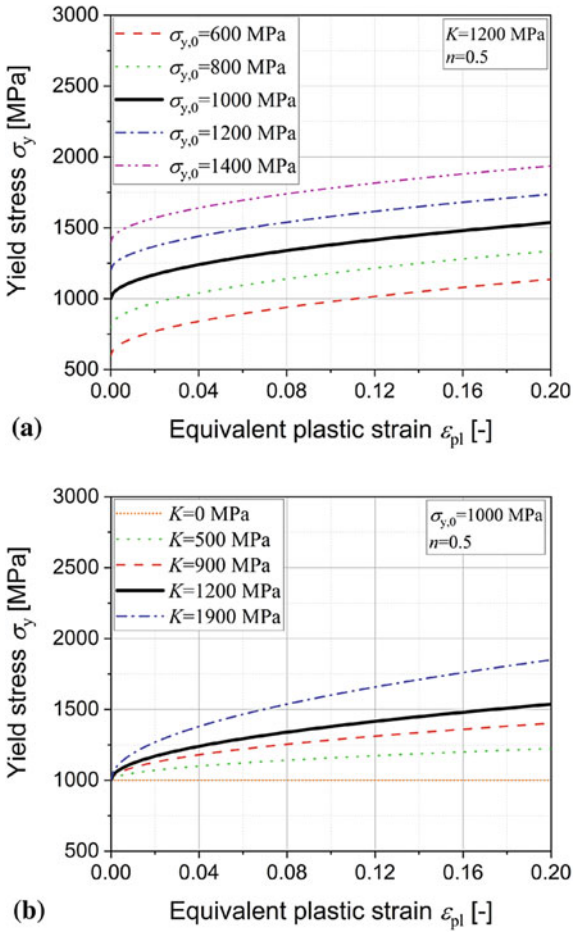

Fig. 6.4 Yield stress as function of equivalent plastic strain according to Eq. (6.2) and corresponding model parameters. While in (**a**) only the initial yield stress $\sigma_{y,0}$ is changed, in (**b**) the strength coefficient K is changed. The strain hardening exponent n remained constant at 0.5

fied by means of thermal desorption spectroscopy (TDS) [10, 28, 42]. An effective "two-trap" approach was applied in the present study considering shallow and deep trapping sites. The binding energies of the shallow and deep trapping sites, respectively, assumed to be $E_{B,shallow} = 30$ kJ/mol and $E_{B,deep} = 60$ kJ/mol. The shallow trapping sites represent mixed dislocations or subgrain boundaries (misorientation less than 15°). Deep trapping sites can be introduced into the microstructure by vacancies or carbide interfaces. Note that carbides not only add deep trapping sites, they also add high densities of shallow trapping sites. The initial trap densities for the shallow and deep trapping sites are both assumed to be $N_{T,0} = 10^{-10}$ mol/mm^3. Only the trap density of the shallow trapping sites evolves during plastic deformation at room temperature according to Eq. (6.7). Due to the high binding energy of the deep trapping sites, the equilibrium constant is approximately unity and all reversible deep trapping sites are fully occupied by hydrogen at room temperature.

Table 6.1 Summary of the model parameters. The parameters for the stress–strain curves can be found in Fig. 6.4

Parameter	Symbol	Value	Uni	References
Tracer diffusion coefficient	D_L	$9 \cdot 10^{-3}$	mm^2/s	[24, 43]
Shallow binding energy	$E_{B,shallow}$	30	kJ/mol	
Deep binding energy	$E_{B,deep}$	60	kJ/mol	
Young's modulus of iron	E	210	GPa	
Correlation factor	κ	$2 \cdot 10^9$	mm^{-2}	[44]
Number of trap sites per unit length of dislocations	k	$7.2 \cdot 10^{-18}$	mol/mm	[17]
Molar mass of hydrogen	M_H	1.008	g/mol	
Density of interstitial lattice sites	N_L	$2 \cdot 10^{-4}$	mol/mm^3	[15]
Shallow trap density	$N_{T,shallow}$	10^{-10}	mol/mm^3	
Deep trap density	$N_{T,deep}$	10^{-10}	mol/mm^3	
Poisson constant of iron	ν	0.3	–	
Density or iron	ρ	$7.9 \cdot 10^{-3}$	g/mm^3	
Partial molar volume	V_H	$1.2 \cdot 10^{-3}$	mm^3/mol	[45]

Therefore, increasing the binding energy of the deep trapping sites would not change the simulation results. Finally, all mechanical and diffusional model parameters are summarized in Table 6.1.

6.5 Results and Discussion

6.5.1 Modeling of Gaseous and Electrochemical Pre-charging

An initial total hydrogen concentration of $c = 0.2$ wppm is considered in the FE simulations. This low concentration should represent, e.g., corrosive hydrogen uptake of advanced high-strength steels during service. The initial hydrogen concentration c is homogenously distributed throughout the sample. During the simulations of the SSR tests, hydrogen accumulates at the notch and depletes at the notch flanks. To study the role of "beneficial" deep trapping sites on the hydrogen accumulation during SSR testing, it is assumed that the initial total hydrogen concentration increases during gaseous hydrogen pre-charging and remains unchanged in electrochemically pre-charged samples. Gaseous hydrogen charging occurs under constant outer hydrogen partial pressure at elevated temperatures. The temperature is needed to dissociate the hydrogen molecules and to increase the chemical hydrogen adsorption and the absorption rates. As illustrated in Fig. 6.5a, the outer partial pressure and tempera-

ture define the applied chemical potential. In equilibrium, the chemical potentials μ_L and $\mu_{P_{H_2}}$ of the lattice hydrogen in bulk and of the gaseous hydrogen molecules, respectively, are equal at the surface [46]. Thus, the equilibrium lattice hydrogen concentration c_L depends only on the square root of the outer hydrogen partial pressure $\sqrt{p_{H_2}}$, which is known as Sieverts' law, as

$$c_L = m\sqrt{p_{H_2}}\exp\left(-\frac{E_S}{RT}\right) = \text{const.}, \tag{6.8}$$

with p_{H_2}, E_S and m being the outer hydrogen partial pressure, the solution energy and a constant factor, respectively. This leads to an increase of the initial total hydrogen concentration c by adding deep trapping sites to the microstructure.

Figure 6.5b illustrates the hydrogen uptake via the surface during electrochemical hydrogen charging. It is a complex chemical and electrochemical process. Different chemical and electrochemical reactions including Volmer, Tafel, Heyrovsky, and absorption reactions occur at the surface. These reactions depend strongly on hydrogen charging parameters, such as temperature, electrolyte velocity, thickness of the boundary layer, sample geometry, applied current density, oxide layers, or hydrogen flux to the bulk. In stationary state, the electron transfer via the surface and the concentration of the chemically adsorbed hydrogen H_{ad} are constant. Electrochemical permeation experiments are suitable to estimate the stationary hydrogen absorption flux J, which is approximately 5–10% of the applied current density [18] for a given sample thickness. In a first approximation electrochemical pre-charging can be modeled by assuming constant hydrogen surface flux $J = \text{const.}$ [47, 48]. This leads to a defined total hydrogen concentration in the samples after a charging time t and does not change by adding deep trap sites, as

$$c = JA\frac{t}{V} = \text{const.}, \tag{6.9}$$

where A is the sample surface and V is the sample volume.

6.5.2 *Local Model-Based Evaluation of Notched Tensile Samples*

It is well known that the strain rate dependency of SSR tests depends on different parameters, as the notch geometry or the chemical hydrogen diffusion. Due to localized plastic deformation, the local equivalent strain ε_{eqv} at the notch root differs from the engineering strain ε_{eng} in tension direction:

$$\varepsilon_{eng} = \frac{L - L_0}{L_0}, \tag{6.10}$$

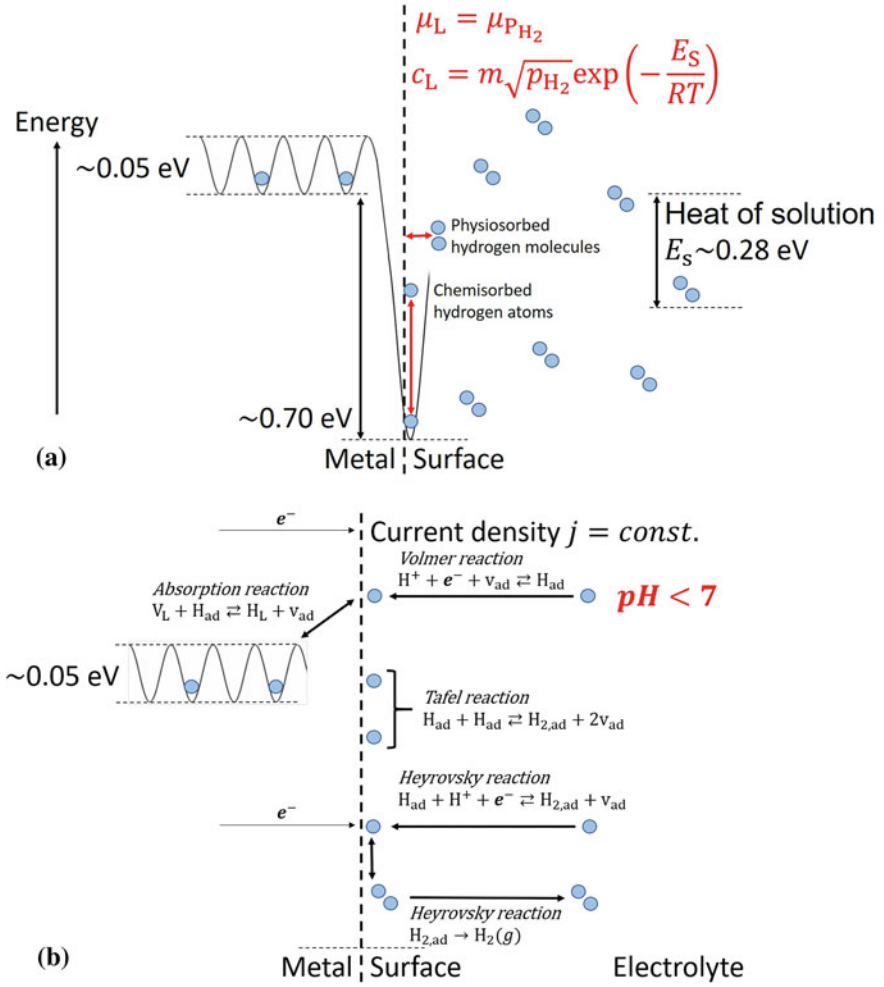

Fig. 6.5 **a** Illustration of the gaseous hydrogen uptake at the metal surface. **b** Illustration of the electrochemical hydrogen uptake at the metal surface in acidic electrolytes (pH < 7)

with $L_0 = 30$ mm being the length of the unstrained gauge section and L being the current length of the gauge section. The equivalent strain ε_{eqv} was evaluated according to von Mises. Figure 6.6 correlates the local equivalent strain at the notch root with the engineering strain ε_{eng}. The local equivalent strain increases faster than the engineering strain. In the linear elastic regime of the sample, the local equivalent strain is about 9 times larger than the engineering strain. With the onset of local plastic deformation, the local equivalent strain increases even faster at the notch root. In other words, the local equivalent strain in the plastically and volumetrically strained zone is a magnitude larger than the engineering strain. The same is true

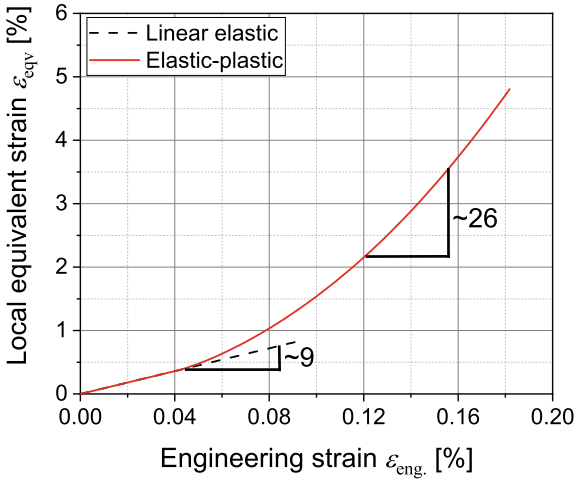

Fig. 6.6 Local equivalent strain at the notch root as function of applied engineering strain for linear elastic and elastic-plastic material behaviors

for the local strain rates. This difference between local and engineering quantities is very important and illustrates the influence of the sample geometry on the SSR test results.

Figure 6.7 shows the distributions of the equivalent plastic strain ε_{pl} and of the hydrostatic stress σ_H , respectively, in the notched sample for an engineering strain of $\varepsilon_{eng} = 0.17$ %. Due to the high initial yield stress of $\sigma_{y,0} = 1000$ MPa with $K = 1200$ MPa and $n = 0.5$, the plastic deformation localizes at the notch. This effect is even more pronounced with increasing yield stress. The zone of the hydrostatic stress rise at the notch is circular shaped. Due to the long-range interactions between hydrogen and volumetrically strained interstitial lattice sites, the hydrostatic stress peak at the notch can even attract hydrogen from the notch flanks and from the surface.

Both the localized equivalent plastic strain ε_{pl} and the hydrostatic stress σ_H influence the hydrogen redistribution during SSR testing of notched and hydrogen precharged samples. According to Eq. (6.7), the trap density increases linearly with increasing equivalent plastic strain at the notch, as shown in Fig. 6.8a. Trapping at the various lattice defects created by equivalent plastic strain and stress concentration causes local hydrogen accumulation with a maximum at the notch root. Due to the isolated surface conditions, e.g., by means of galvanization after hydrogen precharging, hydrogen redistributes at the notch, as shown in Fig. 6.8b. As expected, most of the hydrogen is provided from the notch flanks and from the surface areas. To understand the strain rate dependency of the hydrogen accumulation due to hydrogen diffusion, the theoretical concept of chemical diffusion must be considered. The chemical diffusion coefficient D_{chem} links the chemical hydrogen flux $J_{\nabla c}$ with the gradient of the total hydrogen concentration ∇c [49] instead of the gradient of the

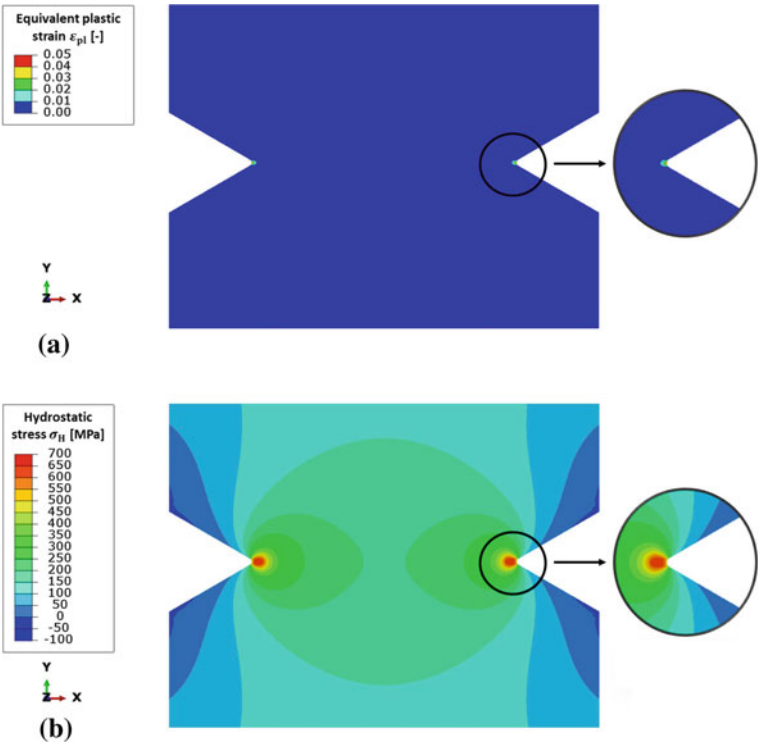

Fig. 6.7 **a** Equivalent plastic strain and **b** hydrostatic stress in the notched sample for an engineering strain of 0.17 % and a corresponding nominal stress of 600 MPa

lattice hydrogen concentration ∇c_L, as in Eq. (6.3). The chemical diffusion coefficient is defined as

$$D_{\text{chem}} = D_L \frac{\partial c_L}{\partial c}. \tag{6.11}$$

In general, D_{chem} differs from the tracer diffusion coefficient D_L, as used in Eq. (6.3), and from the effective diffusion coefficient D_{eff} [15, 28, 35, 50]. Due to the thermodynamic factor $\frac{\partial c_L}{\partial c}$, the chemical hydrogen diffusion coefficient depends on the local hydrogen concentration and on the trap density and it varies in the sample, especially in the plastically and volumetrically strained zone at the notch root. D_{chem} increases with increasing hydrogen concentration c of the reversible hydrogen trapping sites, decreases with temperature and decreases with plastic deformation. A decrease of D_{chem} would retard the hydrogen accumulation and most likely increases the strain rate dependency of the SSR tests. As shown in Fig. 6.8c, only at a very small area at the notch root D_{chem} decreases about 10%.

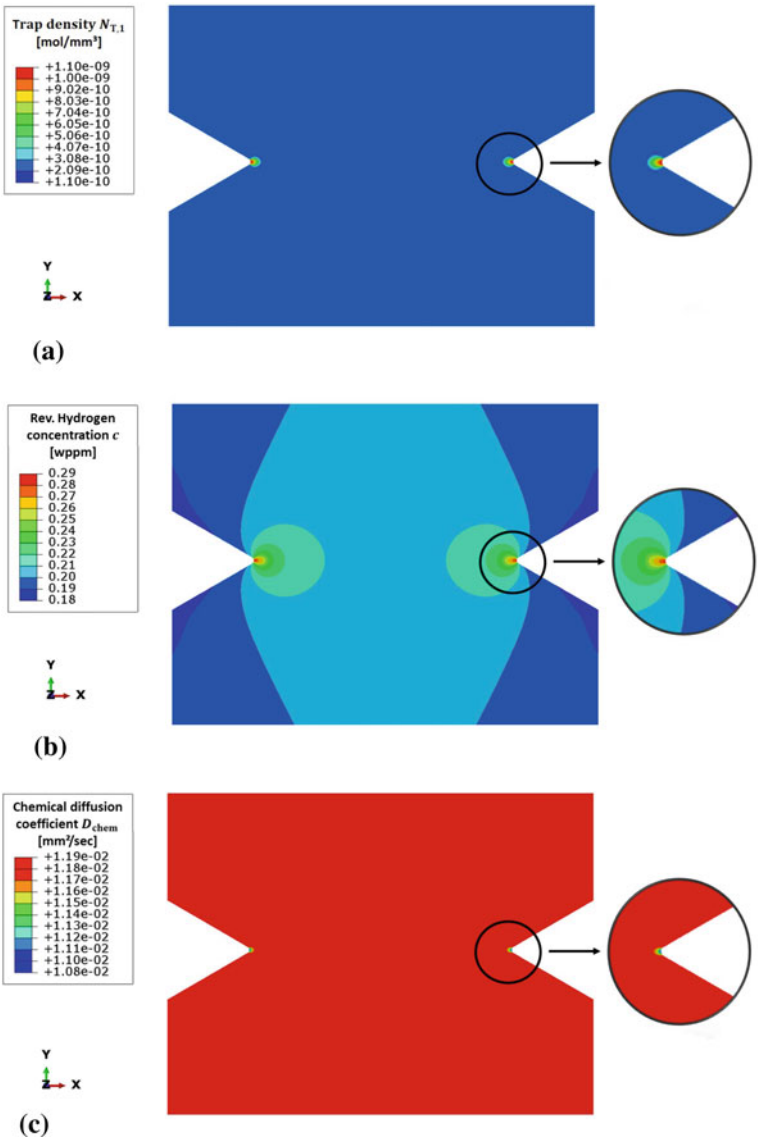

Fig. 6.8 **a** Trap density of reversible shallow trapping sites, **b** reversible total hydrogen concentration and **c** chemical diffusion coefficient D_{chem} in the notched sample for the engineering strain of 0.17%, the strain rate of 10^{-8} 1/s and the initial homogenously distributed total hydrogen concentration of $c = 0.2$ wppm

6.5.3 *Influence of Hydrostatic Stress and Hydrogen Trapping*

Due to the notch effect, stress concentration occurs at the notch. The degree of stress concentration under typically tension loads can be expressed as a non-dimensional stress concentration factor K_t. Mechanical FE analysis of the notched sample revealed $K_t = 7.5$ in the linear elastic regime. Due to the stress concentration, localized plastic deformation starts at the notch root at an engineering stress of $\sigma_{eng} = 130$ MPa and spreads with further increasing tension along the ligament into bulk. This results in the shift of the hydrostatic stress maximum of few micrometers. Figure 6.9 compares the hydrostatic stress profile along the half ligament of the notched sample for a linear elastic and an elastic-plastic material model. Linear elastic simulation revealed the maximum of hydrostatic stress directly at the surface, while elastic-plastic material behavior shifts the maximum of hydrostatic stress from the surface towards the bulk. To compare simulations with identical hydrostatic stress of around 650 MPa, the linear elastic and the elastic–plastic simulations were stopped at engineering strains of $\varepsilon_{eng} = 8.6 \cdot 10^{-2}\%$ and $\varepsilon_{eng} = 0.17\%$, respectively.

Owing to the misfit of the interstitial hydrogen atoms at nanoscale, lattice hydrogen segregates in volumetrically strained areas. This mechanism is well known as stress-driven hydrogen diffusion [51]. To estimate the equilibrium lattice hydrogen concentration in volumetrically strained areas, the total hydrogen flux, Eq. (6.3), was set to zero, which allows to derive the well-known exponential expression for the lattice hydrogen concentration c_L as function of the hydrostatic stress [10]:

$$\frac{c_L}{c_{L,0}} = \exp\left(-\frac{V_H \sigma_H}{R_g T}\right) = K_{\sigma_H}. \tag{6.12}$$

$c_{L,0}$ is the lattice hydrogen under zero hydrostatic stress which should not be mixed up with the total hydrogen concentration c [1]. Equation (6.12) is similar to the generalized equation of Oriani, Eq. (6.6), with K_{σ_H} as the equilibrium constant for

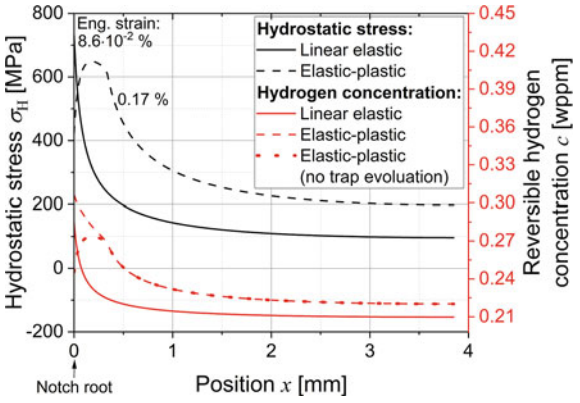

Fig. 6.9 Hydrostatic stress in the ligament of the notched sample and corresponding equilibrium reversible trapped hydrogen concentration according to Eq. (6.12)

volumetrically strained interstitial lattice sites. Comparing $V_H\sigma_H$ with the binding energy E_B of hydrogen trapping sites at microstructural defects gives a corresponding energy of approximately about 1 kJ/mol for a hydrostatic stress of 65 MPa. In addition to the local accumulation of lattice hydrogen, reversible hydrogen trapping reinforces the hydrogen accumulation. Applying Eq. (6.12) together with Eq. (6.6), the equilibrium total reversible hydrogen concentration c can be estimated along the ligament using the simulated hydrostatic stress curve, as shown in Fig. 6.9. The calculations reveal the maximum reversible total hydrogen concentration at the notch root. Neglecting the interaction between plastic deformation and shallow hydrogen trapping, as indicated by the bold dashed line in Fig. 6.9, would shift the maximum of total reversible hydrogen concentration from the surface to the bulk. In this case, the maximum total reversible hydrogen concentration would coincident with the position of the maximum hydrostatic stress. In other words, the localized equivalent plastic deformation and stress concentration at the notch are crucial for understanding hydrogen embrittlement phenomenon on the macroscale.

6.5.4 *Influence of Yield Stress, Strength, and Strain Hardening*

It is well known that the susceptibility of metallic alloys to hydrogen embrittlement [52, 53] increases with increasing strength [54]. In high-strength steels, less than 1 wppm of measured total hydrogen concentration can provoke time-delayed macroscopic brittle failure of structural components. Hydrogen concentrations are always measured on bulk specimens, however, local hydrogen concentrations, e.g., at notches or at severe deformed edges [42], can be 5–10 times higher than the bulk concentrations [42, 55, 56]. In other words, conventional hydrogen analysis techniques cannot distinguish between homogeneous and inhomogeneous hydrogen distributions. Using diffusion-mechanical FE models allows to study the macroscopic influence of the yield stress and of the strain hardening on the local hydrogen accumulation in hydrogen pre-charged and notched samples. Due to the stress concentration and stress triaxiality, the equivalent plastic strain localizes at the notch and reaches higher values than in unnotched tensile samples at equal engineering strains. To study the influence of the initial yield stress on the local hydrogen accumulation, $\sigma_{y,0}$ is increased from 600 MPa to 1400 MPa. The strain hardening was unchanged with $K = 1200$ MPa and $n = 0.5$, as shown in Fig. 6.4a. Figure 6.10 shows the accumulation of total reversible hydrogen concentration as function of initial yield stress and engineering strain rate at an equivalent plastic strain of 3%. Hence, the trap density at the evaluation node is equal in all simulations. With increasing yield stress, the hydrogen accumulation is reduced at the notch root. With decreasing engineering strain rate, the hydrogen accumulation increases and reaches a quasi-static state below 10^{-7} s^{-1}. The local reversible hydrogen concentration increases from an initially homogeneous distributed hydrogen concentration of 0.2 wppm to

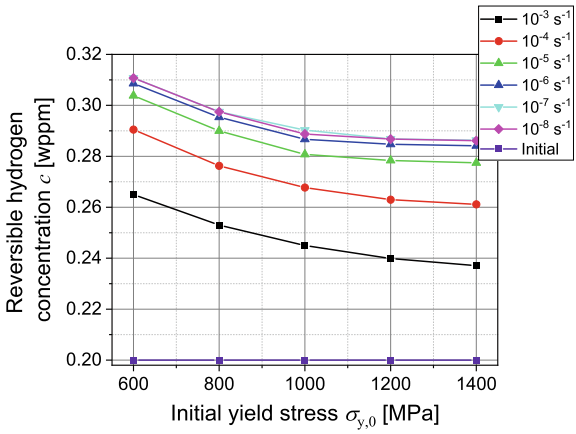

Fig. 6.10 Effect of initial yield stress and strain rate on the local reversible hydrogen concentration at an equivalent plastic strain of 3% at the notch root

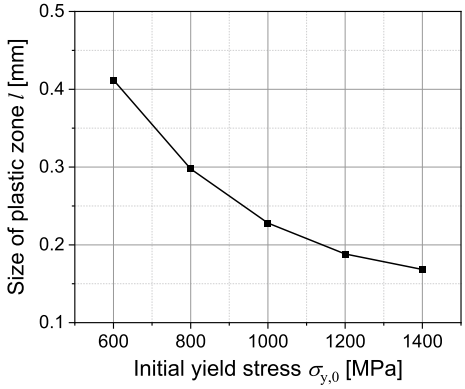

Fig. 6.11 Effect of initial yield stress on plastic localization at the notch root. The size of the plastic zone is given for constant equivalent plastic strain of 3% at the notch root

around 0.31 wppm at $\sigma_{y,0} = 600$ MPa and to around 0.28 at $\sigma_{y,0} = 1400$ MPa. Nevertheless, the influence of the yield stress seems to be more pronounced below $\sigma_{y,0} = 1000$ MPa.

With increasing yield stress, the size of the plastic zone decreases and the maximum of the hydrostatic stress increases. According to Fig. 6.11, the plastic deformation localizes at the notch with increasing yield stress. Comparing simulations at the given equivalent plastic strain of 3%, the size of the plastic zone decreases from 0.41 to 0.18 mm. Due to the higher yield stress and smaller plastic zone, the maximum of the hydrostatic stress increases from 132 MPa to 195 MPa at the maximum equivalent plastic strain of 3%, and the peak position of hydrostatic stress was closer to the surface. In other words, the decrease of the accumulated hydrogen concentration with increasing yield stress can be attributed to the smaller size of the plastic zone and the increasing influence of the stress-driven hydrogen flux pointing from the surface towards bulk.

To evaluate the influence of strain hardening on the local hydrogen accumulation, K is increased from 0 MPa (ideal plasticity) to 1900 MPa. The initial yield stress

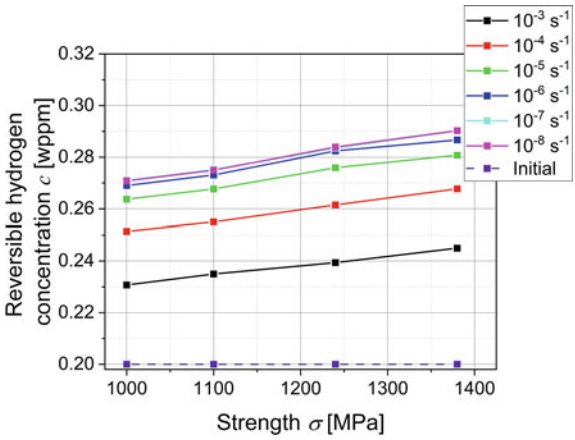

Fig. 6.12 Effect of the strength and strain rate on the local reversible hydrogen concentration at an equivalent plastic strain of 4% at the notch root

is $\sigma_{y,0} = 1000$ MPa, and the strain hardening exponent is $n = 0.5$. The corresponding stress-equivalent plastic strain curves are summarized in Fig. 6.4b. As shown in Fig. 6.12, with increasing strain hardening and thus with increasing strength, more hydrogen accumulates at the notch. The local hydrogen concentrations and strength were evaluated at a local equivalent plastic strain of 4%. Hence, the local shallow trap density at the surface is equal in all simulations. The size of the plastic zone increases slightly from 0.2 to 0.3 mm with increasing strength. The maximum of hydrostatic stress increases with increasing size of plastic deformation from 144 to 191 MPa. However, the increase of the hydrogen concentration at the surface mainly results from the size increase of the plastic zone, which shifts the maximum hydrostatic stress further towards the bulk.

6.5.5 *Influence of "beneficial" Deep Trapping Sites*

Besides the conventional hydrogen solubility in the interstitial lattice sites, atomic hydrogen can trap at foreign substitutional atoms, dislocations, grain boundaries, carbides, microcracks, or micropores [51]. The concept of "beneficial" trapping is very controversial. Only those deep trapping sites, which do not initiate cracks, are beneficial in the sense of hydrogen embrittlement, since strongly trapped hydrogen does not participate in nanoscale hydrogen embrittlement mechanisms. The nature of "beneficial" deep trapping sites is still unexplored, and, e.g., carbides or grain boundaries may increase both deep and shallow trap densities at the same time. To study the "beneficial" effect of deep trapping sites on the hydrogen accumulation at the notch during SSR testing, three cases are compared:

1. Case 1: only shallow trapped hydrogen with a total reversible hydrogen concentration of $c = 0.2$ wppm and a corresponding initial lattice hydrogen concentration of $c_{L,0} = 1.5 \cdot 10^{-9}$ mol/mm^3.
2. Case 2: shallow and deep trapped hydrogen with an initial lattice hydrogen concentration of $c_{L,0} = 1.5 \cdot 10^{-9}$ mol/mm^3 and a total reversible hydrogen concentration of $c = 0.213$ wppm.
3. Case 3: shallow and deep trapped hydrogen with a total hydrogen concentration of $c = 0.2$ wppm and an initial lattice hydrogen concentration of $c_{L,0} = 1.4 \cdot 10^{-9}$ mol/mm^3.

Figures 6.13 and 6.14 show the accumulation of the total reversible hydrogen concentration c at the notch root as function of

1. the engineering strain rate and
2. the equivalent plastic strain.

With decreasing engineering strain rate, hydrogen has more time to diffuse and accumulate locally at the notch. Quasi-static conditions are reached for strain rates below 10^{-7} s^{-1} and the local reversible hydrogen concentration depends only on the equivalent plastic strain. With increasing equivalent plastic strain, the total reversible hydrogen concentration increases. For quasi-static conditions and equivalent plastic strain of 5% at the notch root, the total reversible hydrogen concentration increased from $c = 0.2$ wppm to $c = 0.29$ wppm. Figures 6.13 and 6.14 show the local accumulation of total reversible hydrogen concentration at the notch root with respect to

1. multiple trapping,
2. engineering strain rate,
3. equivalent plastic strain, and
4. hydrogen pre-charging procedure.

While Fig. 6.13 considers gaseous hydrogen pre-charging with $c_{L,0} = 1.5 \cdot 10^{-9}$ mol/mm^3, Fig. 6.14 considers electrochemical hydrogen pre-charging with $c = 0.2$ wppm. With respect to Fig. 6.13 more reversible hydrogen accumulates in the plastically and volumetrically strained zone of gaseous pre-charged samples, but the additional deep trapping sites do not affect the strain rate dependency. The difference to case 1 is exactly 0.013 wppm. Applying electrochemical pre-charging, as shown in Fig. 6.14, causes a decrease of the hydrogen concentration at the notch root compared to gaseous hydrogen pre-charging. This difference is small, but increased slightly with decreasing strain rates. In general, the site fraction $y_{T,deep}$ of the deep trapping sites with the binding energy of $E_{B,deep} = 60$ kJ/mol is almost unity at room temperature. Therefore, gaseous hydrogen pre-charging increases the total reversible hydrogen concentration by $\triangle c = 0.013$ wppm compared to case 1. In addition, the fully occupied deep trapping sits cannot contribute to the chemical diffusion coefficient and remains the engineering strain rate dependency unchanged. Applying electrochemical pre-charging prescribes the total reversible hydrogen concentration.

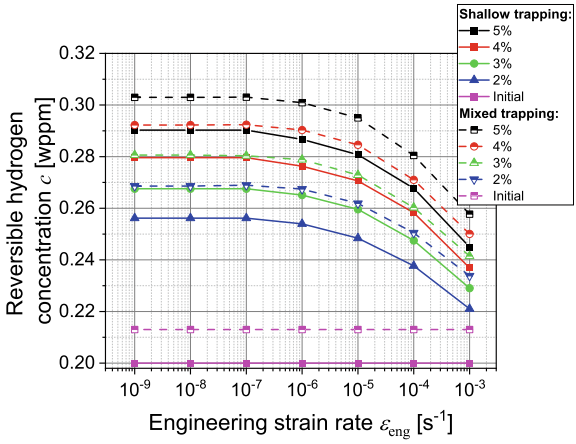

Fig. 6.13 Hydrogen concentration at the notch root as function of engineering strain rate and trapping: shallow hydrogen trapping with binding energy $E_{B,shallow} = 30$ kJ/mol, mixed hydrogen trapping with binding energies $E_{B,shallow} = 30$ kJ/mol and $E_{B,deep} = 60$ kJ/mol and an initial total hydrogen concentration $c = 0.213$ wppm

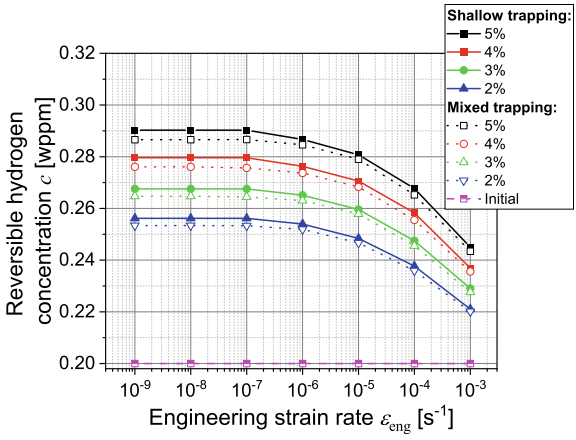

Fig. 6.14 Hydrogen concentration at the notch root as function of engineering strain rate and trapping: shallow hydrogen trapping with binding energy $E_{B,shallow} = 30$ kJ/mol, mixed hydrogen trapping with binding energies $E_{B,shallow} = 30$ kJ/mol and $E_{B,deep} = 60$ kJ/mol and an initial total hydrogen concentration $c = 0.2$ wppm

Therefore, adding deep trapping sites to the microstructure reduces the amount of lattice and shallow trapped hydrogen. Especially, the lower lattice concentration reduces both the stress-driven hydrogen flux and the chemical diffusion coefficient. In other words, the lower lattice hydrogen concentration affects the strain rate dependency during SSR testing, although, the deep trapping sites are fully occupied.

6.6 Conclusion

The following conclusions can be drawn from diffusion-mechanical simulations of slow strain rate (SSR) testing of hydrogen pre-charged and notched samples:

1. The notch effect leads to localized plastic deformation and stress concentration, and increases the local strain rates compared to the global strain rates.

2. Localized plastic deformation during SSR testing shifts the peak position of the hydrostatic stress along the ligament from surface towards bulk, decreases the maximum of the hydrostatic stress and increases the dislocation density and thus the local hydrogen trap density.
3. Due to stress-driven hydrogen diffusion and due to hydrogen segregation to microstructural defects in the plastic zone, internal hydrogen contributes significantly to the strain rate dependency of SSR tests of notched and hydrogen pre-charged samples.
4. The "beneficial" effect of reversible deep trapping sites on the local hydrogen accumulation was studied with respect to strain rate, plastic deformation, multiple trapping, and pre-charging conditions. Deep trapping sites can only reduce the amount of lattice and shallow trapped hydrogen, if hydrogen uptake during pre-charging remains unaffected. Especially, the effect of deep trapping sites on the interstitial lattice hydrogen concentration needs to be further investigated.

References

1. Nagumo, M.: Fundamentals of Hydrogen Embrittlement. Springer Singapore, Singapore (2016)
2. Lynch, S.: Discussion of some recent literature on hydrogen-embrittlement mechanisms: addressing common misunderstandings. Corros. Rev. **37**, 377–395 (2019). https://doi.org/10.1515/corrrev-2019-0017
3. Beachem, C.D.: A new model for hydrogen-assisted cracking (hydrogen "embrittlement"). Metall. Mater. Trans. B. **3**, 441–455 (1972). https://doi.org/10.1007/BF02642048
4. Birnbaum, H.K., Sofronis, P.: Hydrogen-enhanced localized plasticity-a mechanism for hydrogen-related fracture. Mater. Sci. Eng. A. **176**, 191–202 (1994). https://doi.org/10.1016/0921-5093(94)90975-X
5. Troiano, A.R.: The role of hydrogen and other interstitials in the mechanical behavior of metals. Metallogr. Microstruct. Anal. **5**, 557–569 (2016). https://doi.org/10.1007/s13632-016-0319-4
6. Oriani, R.A.: Whitney Award lecture-1987: hydrogen-the Versatile Embrittler. Corrosion **43**, 390–397 (1987). https://doi.org/10.5006/1.3583875
7. Lynch, S.P.: Progress towards understanding mechanisms of hydrogen embrittlement and stress corrosion cracking. NACE Int. Corros. Conf. Ser. **074931–0749355** (2007)
8. Schaffner, T.: Charakterisierung und Modellierung des Wasserstofftransports und der wasserstoffabhängigen Beanspruchungsgrenzen höchstfester Mehrphasenstähle (2018)
9. Barrera, O., Tarleton, E., Tang, H.W., Cocks, A.C.F.: Modelling the coupling between hydrogen diffusion and the mechanical behaviour of metals. Comput. Mater. Sci. **122**, 219–228 (2016). https://doi.org/10.1016/j.commatsci.2016.05.030
10. Drexler, A., Bergmann, C., Manke, G., Kokotin, V., Mraczek, K., Pohl, M., Ecker, W.: On the local evaluation of the hydrogen susceptibility of cold-formed and heat treated advanced high strength steel (AHSS) sheets. Mater. Sci. Eng. A. **800**, 140276 (2021). https://doi.org/10.1016/j.msea.2020.140276
11. Dassault Systèmes Simulia: Abaqus Unified FEA. https://www.3ds.com/products-services/simulia/products/abaqus/
12. Massone, A., Manhard, A., Jacob, W., Drexler, A., Ecker, W., Hohenwarter, A., Wurster, S., Kiener, D.: An SEM compatible plasma cell for in situ studies of hydrogen-material interaction. Rev. Sci. Instrum. **91**, 043705 (2020). https://doi.org/10.1063/1.5142043

13. Cao, Y., Karlsson, B., Ahlström, J.: Temperature and strain rate effects on the mechanical behavior of dual phase steel. Mater. Sci. Eng. A. **636**, 124–132 (2015). https://doi.org/10.1016/j.msea.2015.03.019
14. Koyama, M., Tasan, C.C., Akiyama, E., Tsuzaki, K., Raabe, D.: Hydrogen-assisted decohesion and localized plasticity in dual-phase steel. Acta Mater. **70**, 174–187 (2014). https://doi.org/10.1016/j.actamat.2014.01.048
15. Svoboda, J., Fischer, F.D.: Modelling for hydrogen diffusion in metals with traps revisited. Acta Mater. **60**, 1211–1220 (2012). https://doi.org/10.1016/j.actamat.2011.11.025
16. Fischer, F.D., Svoboda, J., Kozeschnik, E.: Interstitial diffusion in systems with multiple sorts of traps. Model. Simul. Mater. Sci. Eng. **21** (2013). https://doi.org/10.1088/0965-0393/21/2/025008
17. Drexler, A., Siegl, W., Ecker, W., Tkadletz, M., Klösch, G., Schnideritsch, H., Mori, G., Svoboda, J., Fischer, F.D.: Cycled hydrogen permeation through Armco iron—a joint experimental and modeling approach. Corros. Sci. **176**, 109017 (2020). https://doi.org/10.1016/j.corsci.2020.109017
18. Siegl, W., Ecker, W., Klarner, J., Kloesch, G., Mori, G., Drexler, A., Winter, G., Schnideritsch, H.: Hydrogen trapping in heat treated and deformed Armco iron. In: NACE - International Corrosion Conference Series, pp. 1–12 (2019)
19. Kholtobina, A.S., Pippan, R., Romaner, L., Scheiber, D., Ecker, W., Razumovskiy, V.I.: Hydrogen Trapping in bcc Iron. Materials (Basel). **13**, 2288 (2020). https://doi.org/10.3390/ma13102288
20. Counts, W.A., Wolverton, C., Gibala, R.: First-principles energetics of hydrogen traps in α-Fe: point defects. Acta Mater. **58**, 4730–4741 (2010). https://doi.org/10.1016/j.actamat.2010.05.010
21. Kiuchi, K., McLellan, R.B.: The solubility and diffusivity of hydrogen in well-annealed and deformed iron. Acta Metall. **31**, 961–984 (1983). https://doi.org/10.1016/0001-6160(83)90192-X
22. Völkl, J., Alefeld, G.: Diffusion of hydrogen in metals. In: Hydrogen in Metals I. Basic Properties, pp. 321–348 (1978)
23. Liu, X., Xie, W., Chen, W., Zhang, H.: Effects of grain boundary and boundary inclination on hydrogen diffusion in α-iron. J. Mater. Res. **26**, 2735–2743 (2011). https://doi.org/10.1557/jmr.2011.262
24. Hagi, H.: Diffusion coefficient of hydrogen in iron without trapping by dislocations and impurities. Mater. Trans. JIM. **35**, 112–117 (1994). https://doi.org/10.2320/matertrans1989.35.112
25. Toribio, J., Kharin, V.: A generalised model of hydrogen diffusion in metals with multiple trap types. Philos. Mag. **95**, 3429–3451 (2015). https://doi.org/10.1080/14786435.2015.1079660
26. Oriani, R.: The diffusion and trapping of hydrogen in steel. Acta Metall. **18**, 147–157 (1970). https://doi.org/10.1016/0001-6160(70)90078-7
27. Iino, M.: Analysis of irreversible hydrogen trapping. Acta Metall. **30**, 377–383 (1982). https://doi.org/10.1016/0001-6160(82)90217-6
28. Drexler, A., Depover, T., Verbeken, K., Ecker, W.: Model-based interpretation of thermal desorption spectra of Fe–C–Ti alloys. J. Alloys Compd. **789**, 647–657 (2019). https://doi.org/10.1016/j.jallcom.2019.03.102
29. Di Stefano, D., Nazarov, R., Hickel, T., Neugebauer, J., Mrovec, M., Elsässer, C.: First-principles investigation of hydrogen interaction with TiC precipitates in α-Fe. Phys. Rev. B. **93**, 184108 (2016). https://doi.org/10.1103/PhysRevB.93.184108
30. He, Y., Li, Y., Chen, C., Yu, H.: Diffusion coefficient of hydrogen interstitial atom in α-Fe, γ-Fe and ϵ-Fe crystals by first-principle calculations. Int. J. Hydrogen Energy. **42**, 27438–27445 (2017). https://doi.org/10.1016/j.ijhydene.2017.08.212
31. Depover, T., Verbeken, K.: Evaluation of the effect of V_4C_3 precipitates on the hydrogen induced mechanical degradation in Fe-C-V alloys. Mater. Sci. Eng. A. **675**, 299–313 (2016). https://doi.org/10.1016/j.msea.2016.08.053
32. Depover, T., Verbeken, K.: Evaluation of the role of Mo_2C in hydrogen induced ductility loss in Q&T Fe-C-Mo alloys. Int. J. Hydrogen Energy. **41**, 14310–14329 (2016). https://doi.org/10.1016/j.ijhydene.2016.05.176

33. Depover, T., Verbeken, K.: The effect of TiC on the hydrogen induced ductility loss and trapping behavior of Fe-C-Ti alloys. Corros. Sci. **112**, 308–326 (2016). https://doi.org/10.1016/j.corsci.2016.07.013
34. Wallaert, E., Depover, T., Arafin, M., Verbeken, K.: Thermal desorption spectroscopy evaluation of the hydrogen-trapping capacity of NbC and NbN precipitates. Metall. Mater. Trans. A. **45**, 2412–2420 (2014). https://doi.org/10.1007/s11661-013-2181-1
35. Drexler, A., Depover, T., Leitner, S., Verbeken, K., Ecker, W.: Microstructural based hydrogen diffusion and trapping models applied to Fe-C-X alloys. J. Alloys Compd. **826**, 154057 (2020). https://doi.org/10.1016/j.jallcom.2020.154057
36. Drexler, A., Bergmann, C., Manke, G., Kokotin, V., Mraczek, K., Pohl, M., Ecker, W.: On the local evaluation of the hydrogen susceptibility of cold-formed and heat treated advanced high strength steel (AHSS) sheets. Mater. Sci. Eng. A. **800** (2021). https://doi.org/10.1016/j.msea.2020.140276
37. Song, E.J., Suh, D.W., Bhadeshia, H.K.D.H.: Theory for hydrogen desorption in ferritic steel. Comput. Mater. Sci. **79**, 36–44 (2013). https://doi.org/10.1016/j.commatsci.2013.06.008
38. Somerday, B.P., Dadfarnia, M., Balch, D.K., Nibur, K.A., Cadden, C.H., Sofronis, P.: Hydrogen-assisted crack propagation in austenitic stainless steel fusion welds. Metall. Mater. Trans. A. **40**, 2350–2362 (2009). https://doi.org/10.1007/s11661-009-9922-1
39. Kumnick, A.J., Johnson, H.H.: Deep trapping states for hydrogen in deformed iron. Acta Metall. **28**, 33–39 (1980). https://doi.org/10.1016/0001-6160(80)90038-3
40. Drexler, A., Ecker, W., Winzer, N., Mraczek, K., Kokotin, V., Manke, G., Bergmann, C.: A step towards numerical evaluation of the local hydrogen susceptibility of punched and cold-formed advanced high strength steel (AHSS) sheets. In: SteelyHydrogen, p. A02 (2018)
41. Jiang, D.E., Carter, E.A.: Diffusion of interstitial hydrogen into and through bcc Fe from first principles. Phys. Rev. B. **70**, 064102 (2004). https://doi.org/10.1103/PhysRevB.70.064102
42. Drexler, A., Bergmann, C., Kokotin, V., Mraczek, K., Manke, G., Leitner, S., Pohl, M., Ecker, W.: Local hydrogen accumulation after cold forming and heat treatment in punched advanced high strength steel sheets. J. Alloys Compd. 158226 (2020). https://doi.org/10.1016/j.jallcom.2020.158226
43. Grabke, H.J., Riecke, E.: Absorption and diffusion AF hydrogen in steels. Mater. Tehnol. **34**, 331–342 (2000)
44. Novak, P., Ritchie, R.O., Sofronis, P., Somerday, B.P., Yuan, R.: A statistical, physical-based, micro-mechanical model of hydrogen-induced intergranular fracture in steel. J. Mech. Phys. Solids. **58**, 206–226 (2009). https://doi.org/10.1016/j.jmps.2009.10.005
45. Hirth, J.P.: Effects of hydrogen on the properties of iron and steel. Metall. Trans. A. **11**, 861–890 (1980). https://doi.org/10.1007/BF02654700
46. Fischer, F.D., Svoboda, J.: Formation of bubbles by hydrogen attack and elastic-plastic deformation of the matrix. Int. J. Plast. **63**, 110–123 (2014). https://doi.org/10.1016/j.ijplas.2013.10.007
47. Vecchi, L., Simillion, H., Montoya, R., Van Laethem, D., Van den Eeckhout, E., Verbeken, K., Terryn, H., Deconinck, J., Van Ingelgem, Y.: Modelling of hydrogen permeation experiments in iron alloys: characterization of the accessible parameters - Part I - The entry side. Electrochem. Acta. **262**, 57–65 (2018). https://doi.org/10.1016/j.electacta.2017.12.172
48. Vecchi, L., Simillion, H., Montoya, R., Van Laethem, D., Van den Eeckhout, E., Verbeken, K., Terryn, H., Deconinck, J., Van Ingelgem, Y.: Modelling of hydrogen permeation experiments in iron alloys: Characterization of the accessible parameters - Part II - The exit side. Electrochem. Acta. **262**, 153–161 (2018). https://doi.org/10.1016/j.electacta.2017.12.173
49. Kirchheim, R.: Solid solutions of hydrogen in complex materials. In: Solid State Physics - Advances in Research and Applications, pp. 203–291 (2004)
50. Svoboda, J., Mori, G., Prethaler, A., Fischer, F.D.: Determination of trapping parameters and the chemical diffusion coefficient from hydrogen permeation experiments. Corros. Sci. **82**, 93–100 (2014). https://doi.org/10.1016/j.corsci.2014.01.002
51. Drexler, A., He, S., Razumovskiy, V., Romaner, L., Ecker, W., Pippan, R.: Verification of the generalized chemical potential for stress driven hydrogen diffusion in nickel. Philos. Mag. Lett. **100**, 513–523 (2020). https://doi.org/10.1080/09500839.2020.1808253

52. Scully, J.R., Young, G.A., Smith, S.W.: Hydrogen embrittlement of aluminum and aluminum-based alloys. In: Gaseous Hydrogen Embrittlement of Materials in Energy Technologiesm, pp. 707–768. Elsevier (2012)
53. Venezuela, J., Liu, Q., Zhang, M., Zhou, Q., Atrens, A.: A review of hydrogen embrittlement of martensitic advanced high-strength steels. Corros. Rev. **34**, 153–186 (2016). https://doi.org/10.1515/corrrev-2016-0006
54. Yamamoto, S.: Delayed fracture. Tetsu-to-Hagane **55**, 326–337 (1969). https://doi.org/10.2355/tetsutohagane1955.55.4_326
55. Ozdirik, B., Suter, T., Hans, U., Depover, T., Verbeken, K., Schmutz, P., Jeurgens, L.P.H., Terryn, H., De Graeve, I.: Study of the hydrogen uptake in deformed steel using the microcapillary cell technique. Corros. Sci. **155**, 55–66 (2019). https://doi.org/10.1016/j.corsci.2019.04.029
56. Polyanskiy, V.A., Belyaev, A.K., Alekseeva, E.L., Polyanskiy, A.M., Tretyakov, D.A., Yakovlev, Y.A.: Phenomenon of skin effect in metals due to hydrogen absorption. Contin. Mech. Thermodyn. **31**, 1961–1975 (2019). https://doi.org/10.1007/s00161-019-00839-2